

# Giant Electron-Phonon Coupling Induced Band-Gap Renormalization in Anharmonic Silver Chalcohalide Antiperovskites

Pol Benítez,<sup>1,2</sup> Siyu Chen,<sup>3,4</sup> Ruoshi Jiang,<sup>3</sup> Cibrán López,<sup>1,2</sup> Josep-Lluís Tamarit,<sup>1,2</sup> Jorge Íñiguez-González,<sup>5,6</sup> Edgardo Saucedo,<sup>2,7</sup> Bartomeu Monserrat,<sup>3,4</sup> and Claudio Cazorla<sup>1,2</sup>

<sup>1</sup>*Group of Characterization of Materials, Departament de Física, Universitat Politècnica de Catalunya, Campus Diagonal Besòs, Av. Eduard Maristany 10-14, 08019 Barcelona, Spain*

<sup>2</sup>*Research Center in Multiscale Science and Engineering, Universitat Politècnica de Catalunya, Campus Diagonal-Besòs, Av. Eduard Maristany 10-14, 08019 Barcelona, Spain*

<sup>3</sup>*Department of Materials Science and Metallurgy, University of Cambridge, Cambridge CB30FS, UK*

<sup>4</sup>*Cavendish Laboratory, University of Cambridge, Cambridge CB30HE, UK*

<sup>5</sup>*Materials Research and Technology Department, Luxembourg Institute of Science and Technology (LIST),*

*Avenue des Hauts-Fourneaux 5, L-4362 Esch/Alzette, Luxembourg*

<sup>6</sup>*Department of Physics and Materials Science, University of Luxembourg, 41 Rue du Brill, L-4422 Belvaux, Luxembourg*

<sup>7</sup>*Micro and Nanotechnologies Group, Emerging Thin Film Photovoltaics Lab, Departament d'Enginyeria Electrònica, Universitat Politècnica de Catalunya, Campus Diagonal Besòs, Av. Eduard Maristany 10-14, 08019 Barcelona, Spain.*

**Abstract.** Silver chalcohalide antiperovskites (CAP),  $\text{Ag}_3\text{XY}$  ( $X = \text{S}, \text{Se}; Y = \text{Br}, \text{I}$ ), are a family of highly anharmonic inorganic compounds with great potential for energy applications. However, a substantial and unresolved discrepancy exists between the optoelectronic properties predicted by theoretical first-principles methods and those measured experimentally at room temperature, hindering the fundamental understanding and rational engineering of CAP. In this work, we employ density functional theory, tight-binding calculations, and anharmonic Fröhlich theory to investigate the optoelectronic properties of CAP at finite temperatures. Near room temperature, we observe a giant band-gap ( $E_g$ ) reduction of approximately 20–60% relative to the value calculated at  $T = 0$  K, bringing the estimated  $E_g$  into excellent agreement with experimental measurements. This relative  $T$ -induced band-gap renormalization is roughly twice the largest value previously reported in the literature for similar temperature ranges. Low-energy optical polar phonon modes, which break inversion symmetry and promote the overlap between silver and chalcogen  $s$  electronic orbitals in the conduction band, are identified as the primary contributors to this giant  $E_g$  reduction. Furthermore, when considering temperature effects, the optical absorption coefficient of CAP increases by nearly an order of magnitude for visible light frequencies. These insights not only bridge a crucial gap between theory and experiment but also open pathways for future technologies where temperature, electric fields, or light dynamically tailor optoelectronic behavior, positioning CAP as a versatile platform for next-generation energy applications.

**Keywords:** electron-phonon coupling, first-principles calculations, chalcohalide antiperovskites, optoelectronic properties, anharmonicity, Fröhlich theory

## INTRODUCTION

Electron-phonon coupling (EPC), arising from the interactions between electrons and lattice vibrations, is ubiquitous in materials and responsible for a wide range of condensed matter physical effects [1–3]. For example, EPC plays a crucial role in the temperature ( $T$ ) dependence of electrical resistivity in metals, carrier mobility in semiconductors, optical absorption in indirect band gap semiconductors, and the onset of conventional superconductivity. Additionally, EPC enables the thermalization of hot carriers, influences the phonon dispersion in metals, and determines the  $T$ -dependence of electronic energy bands in solids [4, 5].

Likewise, the band gap ( $E_g$ ) of semiconducting and dielectric materials can be significantly affected by EPC,

typically decreasing with increasing temperature (the so-called Varshni effect [6]). This common  $E_g$  behavior can be explained by the Allen-Heine-Cardona perturbative theory, which attributes it to a larger  $T$ -induced energy increase in the valence band compared to the conduction band due to a greater sensitivity to phonon population variations (i.e., larger second-order electron-phonon coupling constants) [7–9]. Representative examples of this thermal  $E_g$  dependence include diamond, which exhibits a  $\sim 5\%$  band-gap reduction at around 1000 K [10, 11]; antimony sulfide ( $\text{Sb}_2\text{S}_3$ ), which shows a  $E_g$  reduction of 200 meV in the temperature range  $10 \leq T \leq 300$  K [12]; and molecular crystals, which display record band-gap reductions of 15–20% at low temperatures [13]. To note that *anomalous* band-gap thermal behaviour, in which  $E_g$  increases with increasing temperature, has also been

observed in a variety of materials such as black phosphorus [14], halide perovskites [15], and chalcopyrite [16] and hydride [11] compounds.

Highly anharmonic silver chalcogenide antiperovskites (CAP) [17] with chemical formula  $\text{Ag}_3\text{XY}$  ( $X = \text{S, Se}$ ;  $Y = \text{Br, I}$ ) are structurally similar to the lead halide perovskites (e.g.,  $\text{CsPbI}_3$ ), with the “anti” designation indicating the exchange of anions and cations compared to the typical ionic perovskite arrangement. Analogous to lead halide perovskites, CAP are highly promising materials for energy and optoelectronic applications [18–23], offering low toxicity due to their lead-free composition [24, 25]. The two most extensively studied CAP compounds,  $\text{Ag}_3\text{SBr}$  and  $\text{Ag}_3\text{SI}$ , possess experimentally determined band gaps of approximately 1.0 eV [26, 27], making them favorable for photovoltaic applications. These materials have also been recognized as high temperature superionic conductors [18, 19]. Additionally, CAP have been investigated as potential thermoelectric materials [22, 23] owing to their substantial vibrational anharmonicity and unique charge transport properties [20, 21].

Intriguingly, for both  $\text{Ag}_3\text{SBr}$  and  $\text{Ag}_3\text{SI}$ , there is an enormous disagreement between the  $E_g$  predicted by first-principles methods (at  $T = 0$  K under static lattice conditions) and those measured experimentally at room temperature. In particular, high-level density functional theory (DFT) calculations employing hybrid functionals and including spin-orbit coupling (SOC) effects estimate the band gap of these two archetypal CAP to be 1.8 and 1.4 eV, respectively [26–28]. The  $E_g$  discrepancies between theory and measurements amount to 60–80% of the experimental values (i.e., differences of 0.5–0.8 eV), which are unusually large and call for a careful inspection of the factors causing them.

In this study, we assessed the influence of EPC and temperature effects on the  $E_g$  and optical absorption spectra of CAP using first-principles DFT methods, tight-binding calculations, and anharmonic Fröhlich theory. Near room temperature, our computational investigations revealed a giant  $E_g$  reduction of 20–60% relative to the value calculated at  $T = 0$  K, bringing the estimated band gap into excellent agreement with the experimental values. Low-energy optical polar phonons, which cause large symmetry-breaking structural distortions and promote the overlap between silver and chalcogen  $s$  electronic orbitals in the conduction band, were identified as the primary mechanism driving this substantial  $T$ -induced band-gap reduction. Furthermore, at finite temperatures the optical absorption spectra of CAP were significantly enhanced, in some cases by nearly an order of magnitude. The polar nature of the phonons causing these effects opens up new technological possibilities, where the optoelectronic properties of materials could be effectively manipulated by external electric fields and light.

## RESULTS

The room-temperature phase of both  $\text{Ag}_3\text{SI}$  and  $\text{Ag}_3\text{SBr}$  have been experimentally identified as cubic with space group  $Pm\bar{3}m$  [27, 30–32]. This phase is characterized by a five-atoms unit cell: a chalcogen atom in the center of the cube, halide atoms in each vertex, and silver atoms in the center of each face (Figs. 1a-b). Phonon calculations of this phase within the harmonic approximation ( $T = 0$  K) reveal imaginary phonon branches, thus indicating dynamical instability. However, when phonons are calculated fully accounting for anharmonic effects at finite- $T$  conditions, the resulting phonon spectrum is well-behaved with no signs of instabilities (Fig. 1c) [17]. Thus, the cubic  $Pm\bar{3}m$  phase was considered throughout this work for all CAP.

As discussed in the Introduction, the discrepancies between the experimentally measured (at  $T = 300$  K) and theoretically determined (at  $T = 0$  K) band gaps of  $\text{Ag}_3\text{SBr}$  and  $\text{Ag}_3\text{SI}$  are tremendously large (i.e., 60–80% of the experimental values). Therefore, we investigated their potential causes by assessing the impact of electron-phonon coupling (EPC) and temperature on the band gap of CAP. To this end, we performed first-principles calculations and *ab initio* molecular dynamics (AIMD) simulations based on DFT (Methods). Additionally, to capture long-range EPC effects, we employed anharmonic Fröhlich theory [33–36] considering long-range dipole-dipole interactions and  $T$ -renormalized phonons (Methods). Furthermore, the optical absorption spectra of all CAP were assessed at  $T \neq 0$  K conditions and the main EPC mechanisms underlying the  $E_g$  discrepancies were identified with the help of a tight-binding model.

**EPC band-gap renormalization in CAP.** The  $T$ -renormalized band gap of CAP was calculated like:

$$E_g(T) = E_g(0) + \Delta E_g(T), \quad (1)$$

where  $E_g(0)$  represents the static band gap and the correction term  $\Delta E_g$  can be expressed as the sum of short- ( $S$ ) and long-wavelength ( $L$ ) phonon contributions [34]:

$$\Delta E_g(T) = \Delta E_g^S(T) + \Delta E_g^L(T). \quad (2)$$

The short-wavelength phonon correction was estimated by performing AIMD simulations with a supercell (Methods) and averaging the band-gap value over several generated configurations, namely [33]:

$$\Delta E_g^S(T) = \frac{1}{N} \sum_{k=1}^N E_g(\{\mathbf{R}_k(T)\}) - E_g(0), \quad (3)$$

where  $N$  represents the total number of considered configurations and  $\{\mathbf{R}_k\}$  the atomic positions of the  $k$ -th configuration. In polar materials, there is an additional contribution to the band-gap renormalization stemming

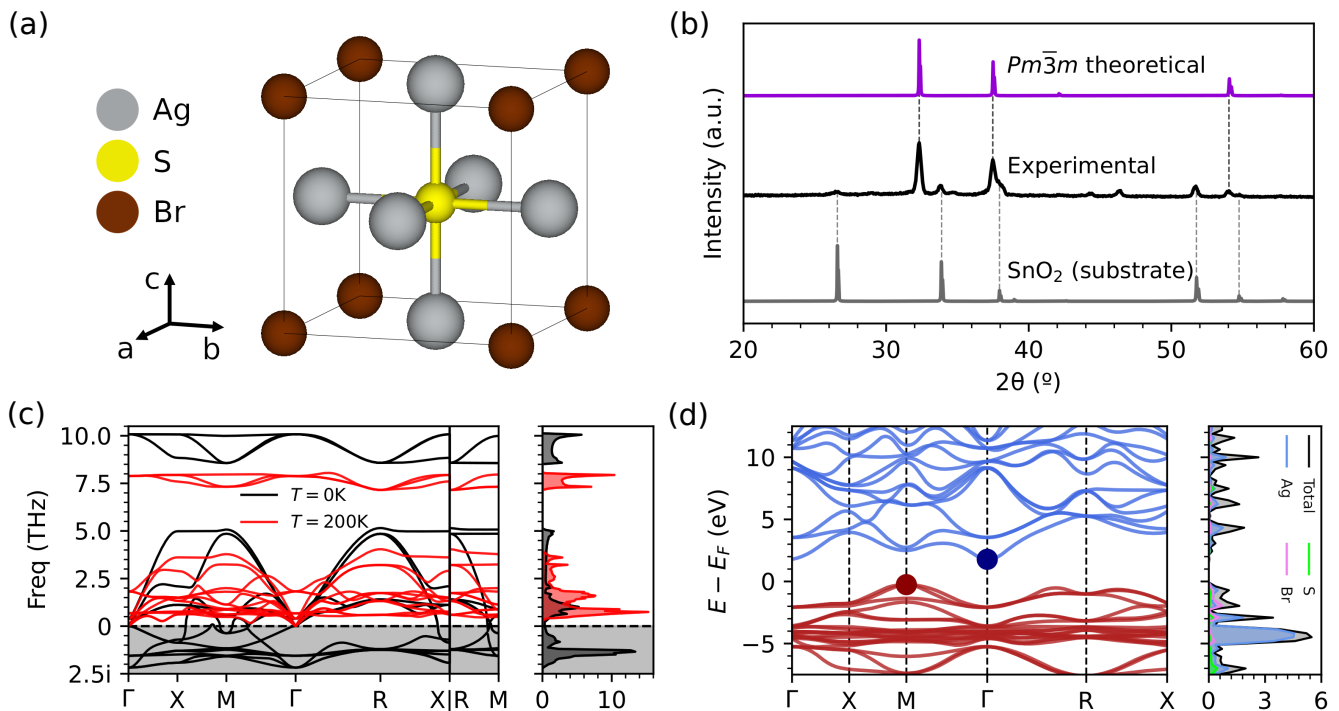


FIG. 1. **General physical properties of the archetypal CAP  $\text{Ag}_3\text{SBr}$ .** (a) The cubic  $Pm\bar{3}m$  phase experimentally observed at room temperature. (b) Experimental diffractogram of  $\text{Ag}_3\text{SBr}$  [27] compared with the theoretical one estimated for the cubic  $Pm\bar{3}m$  phase. (c) Vibrational phonon spectrum (left) and phonon density of states (right) calculated within the harmonic approximation for the cubic  $Pm\bar{3}m$  phase of  $\text{Ag}_3\text{SBr}$  at  $T = 0$  K (black lines) and at  $T = 200$  K (red lines) fully considering anharmonic effects. (d) Electronic band structure (left) and density of states (right) of  $\text{Ag}_3\text{SBr}$  calculated with the hybrid functional HSEsol [29]. Red and blue lines (dots) represent valence (top of the valence) and conduction (bottom of the conduction) bands, respectively.

CAP	$E_g^{0\text{K}}$ [eV]	$E_g^{200\text{K}}$ [eV]	$\Delta E_g^S$ [meV]	$\Delta E_g^L$ [meV]	$E_g^{400\text{K}}$ [eV]	$\Delta E_g^S$ [meV]	$\Delta E_g^L$ [meV]	$E_g^{600\text{K}}$ [eV]	$\Delta E_g^S$ [meV]	$\Delta E_g^L$ [meV]	$E_g^{\text{exp}}$ [eV]
$\text{Ag}_3\text{SBr}$	1.8	$1.3 \pm 0.1$	-440	-32	$1.1 \pm 0.1$	-570	-88	$1.0 \pm 0.2$	-680	-145	1.0
$\text{Ag}_3\text{SI}$	1.4	$1.1 \pm 0.1$	-260	-21	$1.1 \pm 0.1$	-230	-58	$0.8 \pm 0.1$	-490	-95	0.9
$\text{Ag}_3\text{SeBr}$	1.6	$0.9 \pm 0.1$	-630	-32	$0.7 \pm 0.1$	-770	-82	liquid	-	-	-
$\text{Ag}_3\text{SeI}$	1.3	$0.9 \pm 0.1$	-370	-24	$0.8 \pm 0.2$	-400	-61	liquid	-	-	-

TABLE I. **Theoretical band gaps of CAP as a function of temperature.**  $E_g$  values were obtained at zero temperature (excluding quantum nuclear effects) at  $T = 200, 400,$  and  $600$  K. Calculations were performed at the HSEsol+SOC level [29]. Numerical uncertainties are provided, which mainly result from the  $\Delta E_g^S$  correction term. Short- and long-wavelength phonon band-gap corrections,  $\Delta E_g^S$  and  $\Delta E_g^L$ , respectively, are provided at each temperature (excluding quantum nuclear effects). The experimental band gaps measured at room temperature for  $\text{Ag}_3\text{SBr}$  and  $\text{Ag}_3\text{SI}$  [27] are shown for comparison.

from long-range Fröhlich coupling that is not fully captured by the finite size of the supercells employed in the AIMD simulations [33–37]. This long-wavelength phonon band-gap correction can be expressed as:

$$\Delta E_g^L(T) = \Delta \epsilon_{\text{CB}}^L(T) - \Delta \epsilon_{\text{VB}}^L(T), \quad (4)$$

where CB and VB refer to the bottom conduction and top valence band levels, respectively.

For a 3D polar material, the  $T$ -induced energy level shifts appearing in Eq. (4) can be computed as [33]:

$$\Delta \epsilon_i^L(T) = \frac{2\alpha_P}{\pi} \hbar \omega_{\text{LO}} \tan^{-1} \left( \frac{q_{\text{F}}}{q_{\text{LO},i}} \right) [2n_T + 1], \quad (5)$$

where  $\alpha_P$  represents the polaron constant,  $\omega_{\text{LO}}$  the phonon frequency averaged over the three longitudinal optical  $\Gamma$  phonon modes [37], and  $q_{\text{F}}$  a trunca-

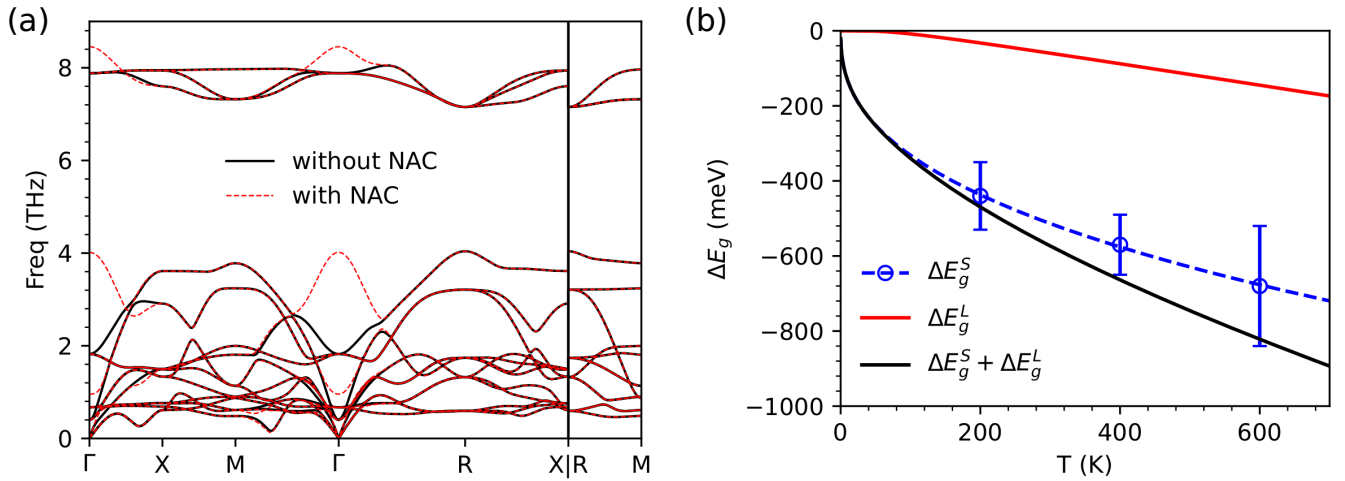


FIG. 2. **Anharmonic phonon spectrum and thermal band-gap corrections estimated for the archetypal CAP  $\text{Ag}_3\text{SBr}$ .** (a) Anharmonic phonon spectrum obtained at  $T = 200$  K neglecting (black solid lines) and considering (red dashed lines) non-analytical corrections (NAC). (b) Short- and long-wavelength phonon band-gap corrections,  $\Delta E_g^S$  and  $\Delta E_g^L$ , respectively, expressed as a function of temperature (excluding quantum nuclear effects). The short-range correction term was evaluated at several temperature points (blue circles and error bars); a power law function was subsequently fitted to the  $\Delta E_g^S$  data (blue dashed line) as a guide to the eye. Calculations were performed at the HSEsol+SOC level [29].

tion factor. The truncation factor  $q_F$  can be approximated as the Debye sphere radius and  $q_{\text{LO},i}$  is defined as  $\sqrt{2m^*(\omega_{\text{LO}} + \omega_i)/\hbar}$ ,  $m^*$  being the charge carrier effective mass and  $\hbar\omega_i$  the state energy. The term  $n_T$  is the Bose-Einstein occupation number corresponding to the average LO vibrational frequency, and the polaron constant can be computed as [33]:

$$\alpha_P = \frac{e^2}{4\pi\epsilon_0\hbar} \left( \frac{1}{\epsilon_\infty} - \frac{1}{\epsilon_0} \right) \left( \frac{m^*}{2\hbar\omega_{\text{LO}}} \right)^{1/2}, \quad (6)$$

where  $\epsilon_\infty$  is the high-frequency dielectric constant and  $\epsilon_0$  the static permittivity of the system. Quantum nuclear effects have been disregarded throughout this work, hence the  $T$ -induced energy level shifts in Eq. (5) were offset by their zero-temperature values  $\Delta E_g^L(0)$ .

Figure 2a presents the anharmonic phonon spectrum calculated for  $\text{Ag}_3\text{SBr}$  under finite-temperature conditions, accounting for long-range dipole-dipole interactions (i.e., including non-analytical corrections), which result in very large LO-TO splitting near the reciprocal space point  $\Gamma$ . Figure 2b shows the corresponding short- and long-wavelength phonon band-gap corrections expressed as a function of temperature, which are always negative. Since in this study the  $\Delta E_g^L$  correction term has been calculated using the material's anharmonic phonon spectrum, we refer to this method as anharmonic Fröhlich theory (Methods).

In Fig. 2b, it is observed that near room temperature the  $\Delta E_g^S$  correction is dominant and significantly larger than  $\Delta E_g^L$ , approximately seven times greater in absolute value. Notably, at  $T = 400$  K, the total band-gap correction for  $\text{Ag}_3\text{SBr}$  amounts to 0.7 eV, which is giant,

representing roughly 40% of the  $E_g$  value calculated at zero temperature (excluding quantum nuclear effects).

Figure 3 shows the relative band-gap variation, referenced to the value calculated at zero temperature and expressed as a function of temperature, for the four CAP compounds  $\text{Ag}_3\text{SBr}$ ,  $\text{Ag}_3\text{SI}$ ,  $\text{Ag}_3\text{SeBr}$  and  $\text{Ag}_3\text{SeI}$ . In all cases, the band gap significantly decreases as the temperature increases (Table I). The relative  $T$ -induced  $E_g$  reduction is largest for  $\text{Ag}_3\text{SeBr}$  and smallest for  $\text{Ag}_3\text{SI}$ . In particular, near room temperature, the band gap of  $\text{Ag}_3\text{SBr}$  and  $\text{Ag}_3\text{SI}$  is reduced by 39% and 21% while those of  $\text{Ag}_3\text{SeBr}$  and  $\text{Ag}_3\text{SeI}$  decrease by 56% and 38%, respectively (Fig. 3). As shown in Table I, the agreement between the experimental and theoretical  $E_g$  values for  $\text{Ag}_3\text{SBr}$  and  $\text{Ag}_3\text{SI}$  improves as the temperature increases. In  $\text{Ag}_3\text{SeBr}$  and  $\text{Ag}_3\text{SeI}$ , the liquid phase is stabilized over the crystal phase at moderate temperatures (Fig. 3c-d), thus no band gaps were estimated for these two compounds at  $T > 400$  K conditions.

Notably, our theoretical  $E_g$  results obtained at  $T = 400$  K are fully consistent with the available experimental data obtained at room temperature. This excellent agreement near ambient conditions strongly suggests that the neglect of EPC effects is the main reason for the huge theoretical-experimental  $E_g$  discrepancies discussed in the Introduction. The  $T$ -induced relative band-gap renormalizations found in CAP are giant, ranging from 20 to 60% near room temperature, setting a new record previously held by molecular crystals, which exhibited a 15 to 20% band-gap renormalization for similar temperature ranges [13].

Table I also presents the value of the  $\Delta E_g^S$  and  $\Delta E_g^L$  correction terms estimated for each CAP at three

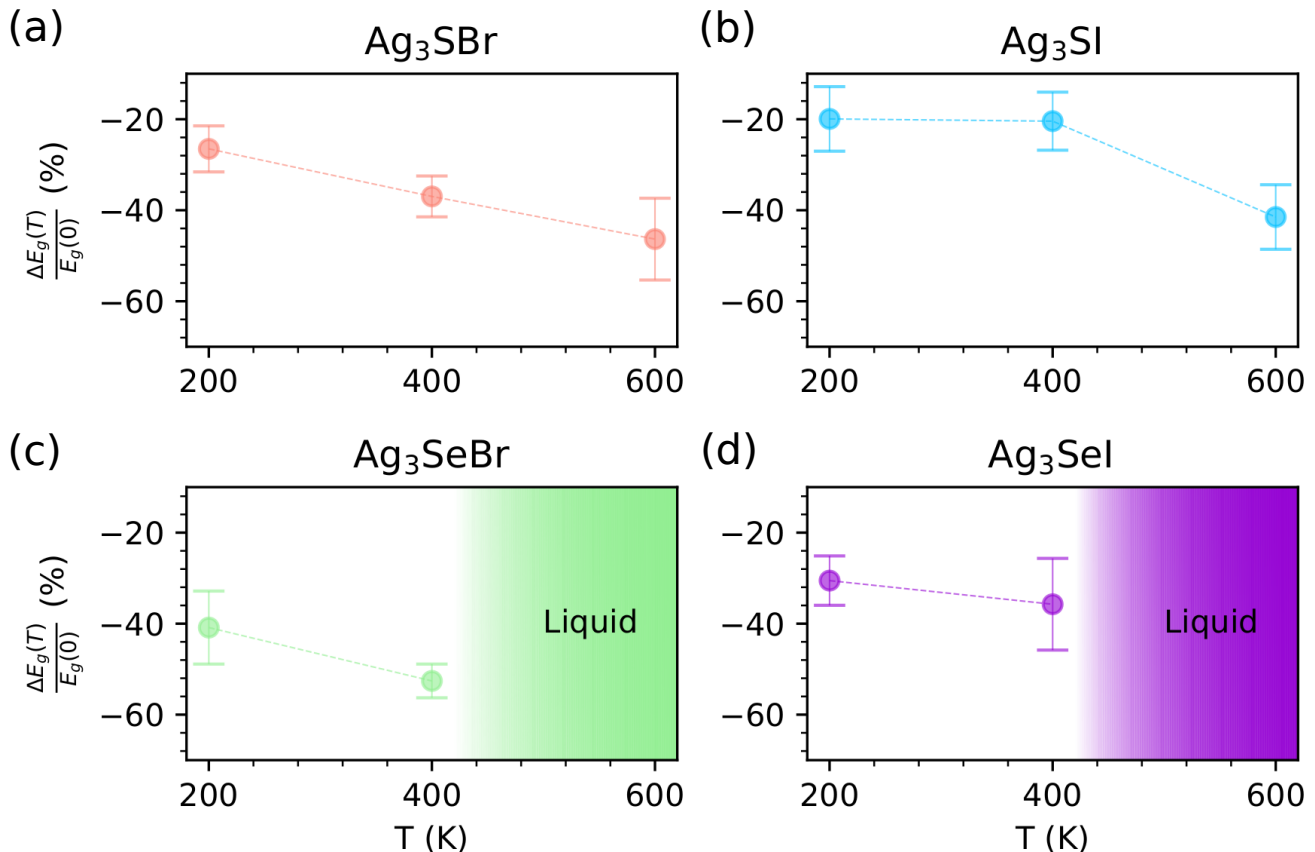


FIG. 3. **Temperature-induced relative band-gap variation in CAP.** Percentages are referenced to the band gap calculated at  $T = 0$  K conditions (excluding quantum nuclear effects), namely,  $\Delta E_g(T) = E_g(T) - E_g(0)$ , for (a) Ag<sub>3</sub>SBr, (b) Ag<sub>3</sub>SI, (c) Ag<sub>3</sub>SeBr, and (d) Ag<sub>3</sub>SeI. Error bars indicate numerical uncertainties and dashed lines are guides to the eye. Shaded areas indicate regions of thermodynamic stability of the liquid phase (theory). Calculations were performed at the HSEsol+SOC level [29].

different temperatures. In all cases, both the short- and long-wavelength phonon corrections are negative, with the former term considerably surpassing the latter in absolute value. For example, at  $T = 400$  K, the short-range band-gap corrections are nine and four times larger than the long-range ones calculated for Ag<sub>3</sub>SeBr and Ag<sub>3</sub>SI, respectively. As the temperature is raised, the size of the two band-gap correction terms increase in absolute value, with  $|\Delta E_g^L|$  exhibiting the largest relative enhancement (e.g., approximately a 450% increase for Ag<sub>3</sub>SBr from 200 to 600 K).

**$T$ -effects on the optical absorption coefficient of CAP.** Following a similar approach to that used for the calculation of  $T$ -renormalized band gaps (i.e., performing AIMD simulations with a supercell and averaging the quantity of interest over several of the generated configurations), we determined the frequency-dependent complex dielectric tensor of CAP under  $T \neq 0$  K conditions, employing linear response theory. From the average dielectric tensor, we computed several macroscopic optical

properties like the optical absorption coefficient,  $\alpha(\omega)$ , refractive index, and reflectivity [38].

Figure 4 shows the optical absorption spectra estimated for CAP as a function of incident light wavelength and temperature. It is found that  $\alpha$  is significantly enhanced under increasing temperature, in some cases by as much as an order of magnitude. Similarly to the band gap, the  $T$ -induced optical absorption variations are largest for Ag<sub>3</sub>SeBr (for which  $\alpha \sim 10^3$ – $10^5$  at zero temperature and  $\sim 10^4$ – $10^6$  cm<sup>-1</sup> at 200 K) and smallest for Ag<sub>3</sub>SI (for which  $\alpha \sim 10^3$ – $10^5$  cm<sup>-1</sup> at any temperature). It is also noted that the most significant optical absorption changes generally occur at low temperatures, that is, within the 0 to 200 K interval. These  $T$ -induced  $\alpha$  trends align well with the remarkably large influence of EPC on the band gap, underscoring the critical role of thermal renormalization effects on the optoelectronic properties of CAP.

Unfortunately, we cannot directly compare our theoretical  $\alpha(\omega)$  results with experimental data, as such data is not available in the literature. Notably, Caño *et*

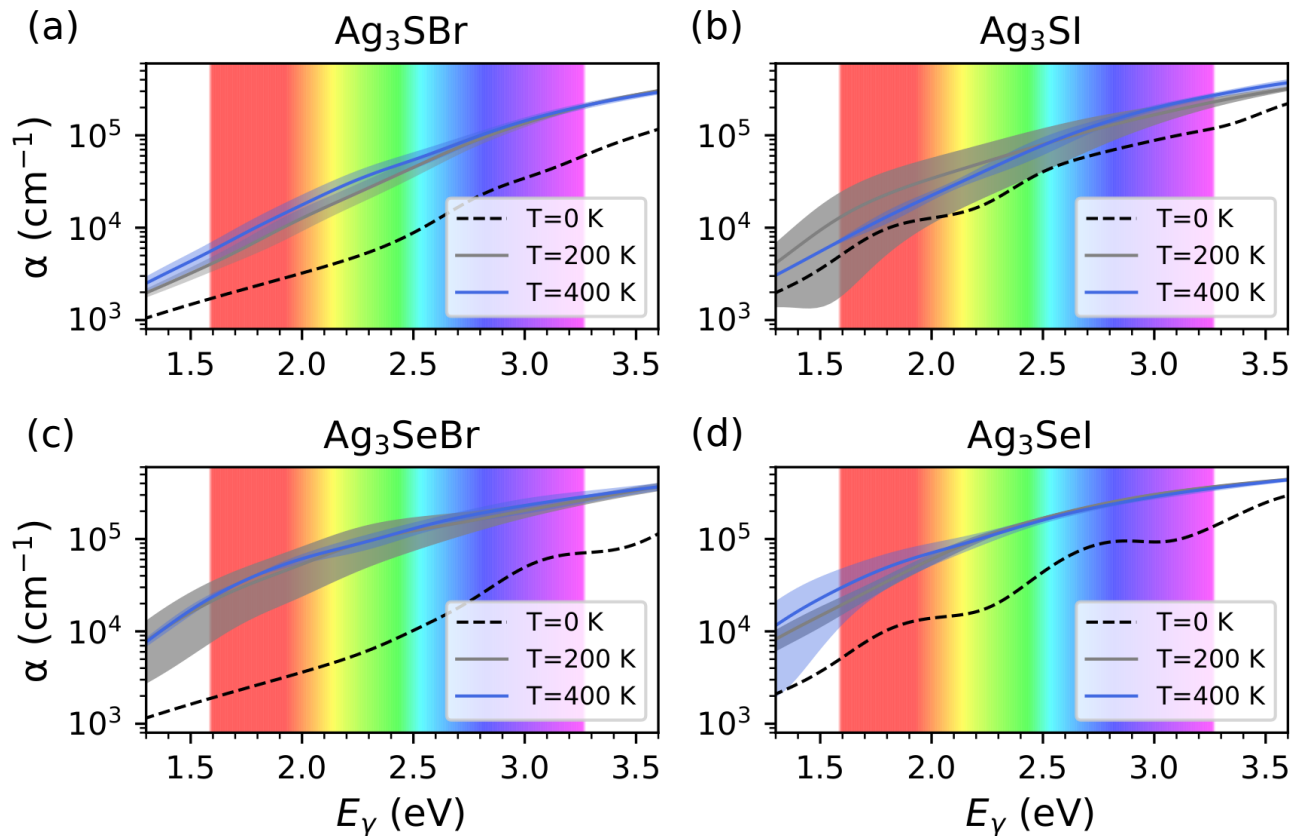


FIG. 4. **Optical absorption coefficient ( $\alpha$ ) of CAP calculated at different temperatures as a function of photon energy.** (a)  $\text{Ag}_3\text{SBr}$ , (b)  $\text{Ag}_3\text{SI}$ , (c)  $\text{Ag}_3\text{SeBr}$ , and (d)  $\text{Ag}_3\text{SeI}$ . Solid lines represent the estimated average values and statistical errors are indicated with shaded thick curves. The rainbow-colored region denotes photons with energy in the visible spectrum. Calculations were performed at the HSEsol+SOC level [29].

*al.* [27] measured the optical absorption coefficient of CAP films scaled by their layer thickness,  $d$ , specifically,  $\bar{\alpha} \equiv \alpha \cdot d$ . However, since the thickness of the synthesized CAP films was not determined in work [27], we cannot access the physical quantity of interest. In this regard, performing new optoelectronic experiments on CAP films across a broad range of temperatures, including the low- $T$  regime, would be highly desirable.

**EPC mechanisms in CAP.** We have already shown that EPC effects are essential for understanding the thermal evolution of the optoelectronic properties of CAP and for achieving a consistent agreement between first-principles calculations and room-temperature experiments. Next, we focus on unraveling the primary ionic-electronic mechanisms underlying these key EPC effects.

As shown in Fig. 5a, the influence of each of the fifteen  $\Gamma$  phonon modes on the band gap of  $\text{Ag}_3\text{SBr}$  was analysed by monitoring the change in  $E_g$  driven by frozen-phonon eigenmode distortions of increasing amplitude,  $u$ . The  $\Gamma$  phonons were classified into acoustic (A), optical polar (P) and optical nonpolar (NP), where the P phonons

break the inversion symmetry of the centrosymmetric cubic  $Pm\bar{3}m$  phase. It was found that  $E_g$  is unresponsive to acoustic phonon distortions, as expected, while optical P phonons produce the largest band-gap variations. As the amplitude of the optical phonon distortions increases,  $E_g$  systematically decreases in both the P and NP cases.

Figure 5b shows the value of the derivative of the band gap with respect to the phonon distortion amplitude,  $u$ , expressed as a function of the phonon eigenmode energy (as obtained from  $T$ -renormalised phonon calculations –Methods–). We found that low-energy polar phonon modes ( $\sim 10$  meV) cause the most significant band-gap reductions, followed by high-energy lattice vibrations of the same type ( $\sim 200$  meV). At room temperature, phonon excitations with the lowest energy host the highest populations and, consequently, represent the most characteristic lattice vibrations in the crystal. Therefore, based on the results shown in Figs. 3 and 5, we conclude that low-energy polar phonon modes are primarily responsible for the substantial temperature-induced  $E_g$  reduction reported in this study for CAP compounds.

The eigenmode of the optical P phonon with the low-

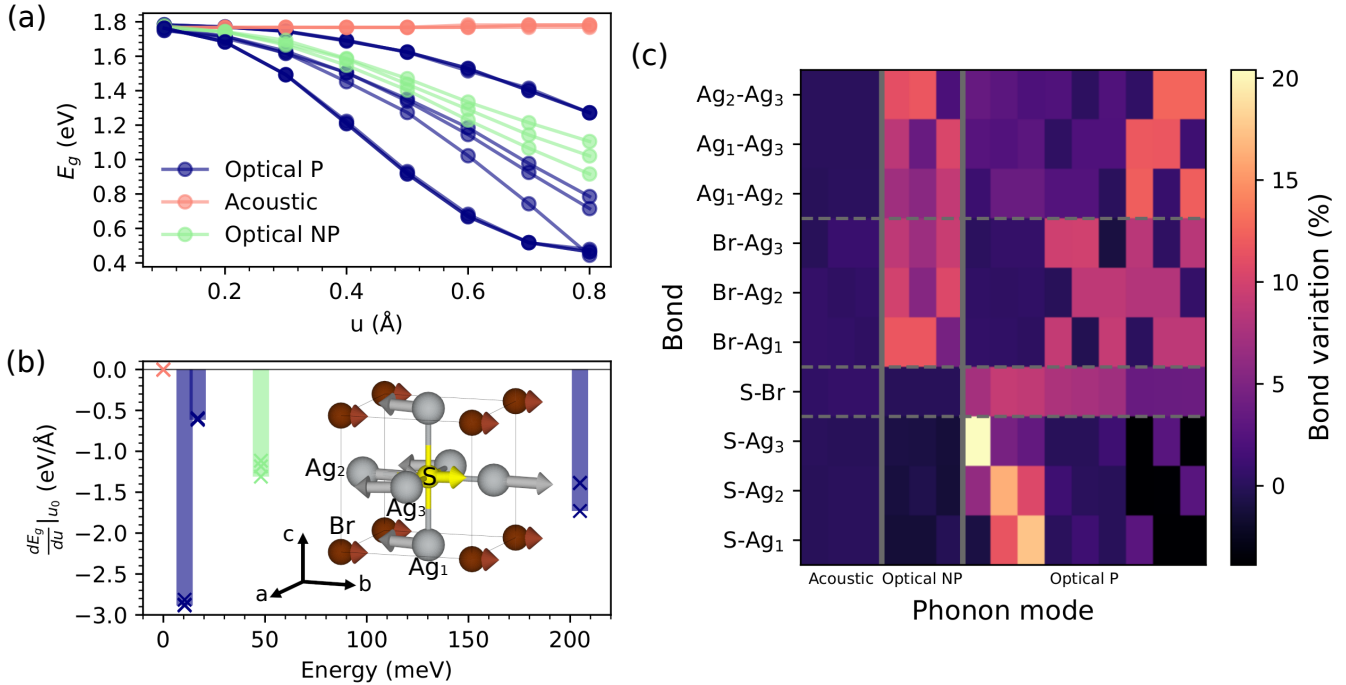


FIG. 5. **Phonon-induced band-gap variation estimated for the archetypal CAP  $\text{Ag}_3\text{SBr}$ .** (a) Band gap as a function of the lattice distortion amplitude  $u$  for acoustic, polar optical (P) and non-polar optical (NP)  $\Gamma$  phonons. (b) Derivative of the band gap with respect to the phonon distortion amplitude calculated at  $u_0 = 0.4 \text{ \AA}$  and expressed as a function of the phonon energy. The eigenmode of the optical polar  $\Gamma$  phonon rendering the largest band-gap derivative in absolute value is sketched: Ag, S and Br atoms are represented with grey, yellow and brown spheres, respectively. Calculations were performed at the HSEsol+SOC level [29]. (c)  $\Gamma$  phonon-induced relative bond length distortions in the cubic  $Pm\bar{3}m$  phase for a distortion amplitude of  $0.4 \text{ \AA}$ .

est energy is represented in Fig. 5b. As observed therein, this frozen-phonon lattice distortion reduces the distance between the central sulfur atom and one adjacent silver atom (Ag2), while increasing the other two S–Ag1 and S–Ag3 bond lengths, compared to the undistorted cubic unit cell. Figure 5c summarizes the relative bond length variation, in absolute value, for all pairs of atoms resulting from each of the fifteen  $\Gamma$  phonon modes calculated for the cubic  $Pm\bar{3}m$  phase. As shown therein, the optical P phonons produce the largest S–Ag distance changes (up to 20%), while the optical NP phonons cause the largest Br–Ag bond length variations (up to 12%). The Br–Ag bond lengths are also appreciably impacted by the optical P phonons (5–10%). This general behaviour is reminiscent of that observed for optical polar phonons in model perovskite oxides like  $\text{BaTiO}_3$  (with atomic substitutions  $\text{Ag} \leftrightarrow \text{O}$ ,  $\text{S} \leftrightarrow \text{Ti}$  and  $\text{Br} \leftrightarrow \text{Ba}$ ) [39, 40].

After identifying the phonon modes that underpin the giant  $T$ -induced band-gap reduction reported in this study for CAP, specifically low-energy optical P modes, we further analyse the induced changes in the electronic band structure. Figure 6a shows the electronic density of states calculated for the archetypal compound  $\text{Ag}_3\text{SBr}$  (equilibrium geometry). It is observed that the top of the valence band (VB) is dominated by highly hybridized

silver  $d$  and chalcogenide  $p$  electronic orbitals, while the bottom of the conduction band (CB) is dominated by isotropic and more delocalized S and Ag  $s$  orbitals. The electronic band structure in Fig. 6b shows that the VB corresponds to the high-symmetry reciprocal space point  $M (1/2, 1/2, 0)$ , while the CB to the center of the Brillouin zone,  $\Gamma (0, 0, 0)$ , thus the band gap of  $\text{Ag}_3\text{SBr}$  is indirect (we have checked that the same conclusion applies to the rest of CAP analyzed in this study).

The effects on the electronic band structure resulting from a frozen-phonon lattice distortion corresponding to the lowest-energy optical P eigenmode are twofold (Fig. 6b). First, due to the phonon-induced inversion symmetry breaking, the energy band degeneracy at the reciprocal space point  $M$  is lifted. However, the band gap of the system is practically unaffected by this energy degeneracy lifting effect. Second, the CB edge experiences a significant decrease and, as a consequence, the band gap of the system is reduced by approximately 30%. Therefore, we may conclude that the giant  $T$ -induced  $E_g$  reduction reported in this study for CAP is primarily caused by low-energy polar phonon modes that induce a pronounced CB energy decrease.

To better understand the electronic origins of the optical P phonon-induced CB energy lowering, we con-

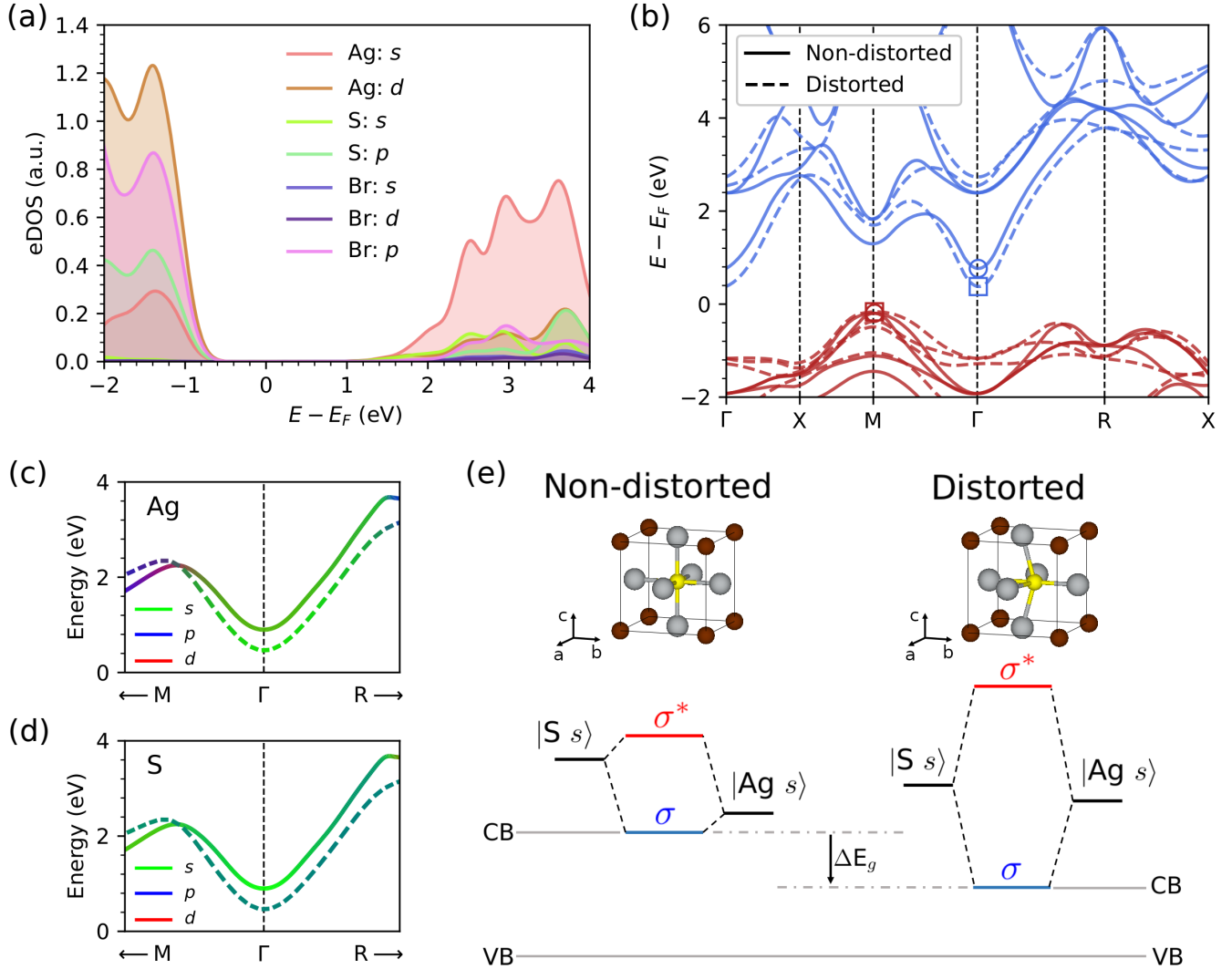


FIG. 6. **Electronic band structure properties of the archetypal CAP  $\text{Ag}_3\text{SBr}$ .** (a) Electronic density of states calculated for the equilibrium cubic  $Pm\bar{3}m$  phase. Partial contributions from different atomic orbitals are indicated. Calculations were performed at the HSEsol+SOC level [29]. (b) Electronic band structure calculated for the equilibrium and phonon distorted (i.e., lowest-energy  $\Gamma$  optical P mode) cubic  $Pm\bar{3}m$  phase; in both cases, the energy bands are referred to a same energy origin, namely, a deep core electronic level that remains unaffected by the distortion (Methods). (c) and (d) The conduction band near its minimum at  $\Gamma$  computed with a TB model for silver and sulfur atoms (Methods); solid and dashed lines correspond to the equilibrium and distorted structures, respectively. (e) Sketch illustrating the mechanism of band-gap closure induced by low-energy polar soft phonon modes in CAP. Upon phonon distortion, the hybridization of silver and sulfur  $s$  electrons in the conduction band is enhanced, lowering (increasing) the energy of the corresponding bonding  $\sigma$  (antibonding  $\sigma^*$ ) state.

structured a tight-binding (TB) model based on Wannier functions that accurately reproduces our DFT band structure results (Methods and Supplementary Fig.1). Specifically, the TB model consists of  $s$ ,  $p$ , and  $d$  orbitals for the five unit-cell atoms, resulting in a total of 45 distinct Wannier orbitals. Consistently, the TB model reproduces the dominant Ag and S  $s$  character of the CB and its energy lowering under the polar lattice distortion of interest (Figs. 6c–d).

According to this TB model, the impact of the frozen-phonon distortion on the Ag and S  $s$  conduction orbitals

is twofold. First, the difference in their kinetic energies, corresponding to the diagonal Hamiltonian matrix elements difference  $|\langle \text{Ag } s | H | \text{Ag } s \rangle - \langle \text{S } s | H | \text{S } s \rangle|$ , decreases (Supplementary Fig.1). And second, the hopping  $s$  term involving the Ag2 and S atoms, represented by the off-diagonal Hamiltonian matrix element  $\langle \text{Ag2 } s | H | \text{S } s \rangle$ , increases (Supplementary Fig.1). Therefore, the general physical interpretation that follows is that the polar frozen-phonon distortion enhances the hybridization of Ag2 and S  $s$  conduction orbitals while simultaneously lowering (increasing) the energy level of the accompany-



ing bonding (antibonding) state  $\sigma$  ( $\sigma^*$ ). The revealed EPC mechanism is schematically illustrated in Fig. 6e.

## DISCUSSION

Thermal expansion is another physical mechanism that can influence the band gap of materials [34], but it was not explicitly considered in this study due to its high computational cost. However, we performed a series of tests in which we arbitrarily increased and decreased the unit cell volume of  $\text{Ag}_3\text{SBr}$  and estimated the corresponding relative  $E_g$  variation (Supplementary Fig.2). We find that, when the volume of the system increases by a reasonable  $\sim 1\%$ , as might occur due to thermal expansion near room temperature, the band gap decreases by only  $\sim 10$  meV (i.e., an order of magnitude smaller change than short-wavelength phonon corrections, Table I). Additionally, thermal expansion likely contributes to the softening of optical P modes, increasing their population and consequently enhancing the  $E_g$  reduction due to EPC. Therefore, while thermal expansion effects were omitted in our calculations, the reported results likely represent a lower bound of the actual effect, and our conclusions for CAP compounds remain robust and accurate.

One may wonder whether, in addition to silver chalcogenide antiperovskites, there may exist other families of materials exhibiting similarly large  $T$ -renormalization effects on the band gap and optical absorption coefficient. As discussed in previous sections, the polar nature of low-energy optical phonons appears to be essential in this regard. Consequently, a tentative set of necessary conditions for identifying potential materials that display similar  $T$ -induced effects on the optoelectronic properties may include dielectric materials exhibiting (1) centrosymmetric crystalline phases, (2) low-energy or even imaginary optical polar phonons, and (3) highly hybridized and delocalized electronic orbitals near the Fermi energy level. The availability of large DFT calculations and phonon databases may enable high-throughput materials screenings of such a kind [41, 42].

Ferroelectric oxide perovskites, exemplified by the archetypal compounds  $\text{SrTiO}_3$  (STO) and  $\text{BaTiO}_3$  (BTO), appear to satisfy the set of necessary conditions outlined above. Notably, a significant band-gap modulation has been reported for STO under biaxial strain conditions, although this phenomenon arises from different physical mechanisms than those identified in this study for CAP, namely, energy degeneracy lifting due to symmetry breaking [43]. Moreover, the experimental room-temperature band gap of BTO ( $\approx 3.2$  eV [44]) shows substantial disagreement with zero-temperature theoretical estimates obtained with hybrid functionals ( $\approx 4.0$  eV [45]), highlighting an experiment-theory inconsistency similar to that described for  $\text{Ag}_3\text{SBr}$  and  $\text{Ag}_3\text{SI}$  in the Introduction. Additionally, the band gap of the multiferroic oxide perovskite  $\text{BiFeO}_3$  exhibits a remarkable temperature-dependent shrinkage, decreasing

by approximately 50% within the temperature range  $300 \leq T \leq 1200$  K [46], likely influenced by the magnetic degrees of freedom [47]. These findings suggest that the electron-phonon coupling mechanisms revealed in this study for CAP compounds may have broader applicability, extending to other families of renowned functional materials.

The polar nature of the optical phonon modes, which cause the significant  $T$ -induced reduction in the  $E_g$  of CAP, opens up exciting technological possibilities. Similar to how an electric field can stabilize a polar phase with ferroelectric polarization over a paraelectric phase at constant temperature through a displacive transformation, it is likely that polar optical phonons in CAP can also be stimulated using external electric fields. This means that the optoelectronic properties of CAP could be efficiently controlled by applying an electric field instead of changing the temperature, offering a more practical method for developing advanced optical devices and other technological applications.

Finally, advances in light sources and time-resolved spectroscopy have made it possible to excite specific atomic vibrations in solids and to observe the resulting changes in their electronic and electron-phonon coupling properties [48–50]. These developments also suggest the possibility of tuning the optoelectronic properties of CAP, as well as of similar materials like oxide perovskites [51–53], through specific phonon excitations using optical means such as lasers. This approach may simplify the design and manufacture of practical setups by eliminating the need for electrode deposition. Therefore, the results presented in this work are significant not only from a fundamental perspective but also for envisioning potential technological applications in which the optical and electronic properties of materials could be effectively tuned by external fields and photoexcitation.

## CONCLUSIONS

In this study, we have explored the temperature effects on the band gap of silver chalcogenide antiperovskites (CAP), specifically  $\text{Ag}_3\text{XY}$  compounds ( $X = \text{S, Se}; Y = \text{Br, I}$ ), which are promising for energy applications due to their lead-free composition, high ionic conductivity, and optoelectronic properties. The key findings of our research are summarized as follows. A giant reduction in the band gap of CAP materials has been disclosed at room temperature, ranging from 20% to 60% relative to their values calculated at zero temperature (neglecting zero-point corrections). This large band-gap renormalization brings theoretical predictions closer to experimental results, resolving previous discrepancies.

The significant  $E_g$  reduction is attributed to strong electron-phonon coupling driven by low-energy polar phonon modes, which distort the lattice symmetry, increase the overlap between silver and chalcogen  $s$  orbitals in the conduction band, and lower the reference energy

of the resulting bonding state. With increasing temperature, the optical absorption coefficient of CAP materials also rises, enhancing their response to visible light by nearly an order of magnitude and highlighting their potential for optoelectronic applications.

This research demonstrates that CAP compounds exhibit giant band-gap renormalization primarily due to electron-phonon coupling effects, suggesting that they could be tailored for specific applications through thermal, electric field, and/or optical control. These fundamental findings open possibilities for the design of innovative optoelectronic devices and establish a foundation for exploring similar effects in other dielectric materials with strong electron-phonon coupling.

## METHODS

**Zero-temperature first-principles calculations.** The DFT calculations [54–56] were performed using the semilocal PBEsol approximation [57], considering the following electronic states as valence: Ag  $5s-4d$ , S  $3s-3p$ , Se  $4s-4p$ , Br  $4s-4p$ , I  $5s-5p$ . Wave functions were represented in a plane-wave basis set truncated at 650 eV. Using these parameters and a dense  $\mathbf{k}$ -point grid of  $8 \times 8 \times 8$  for reciprocal-space Brillouin zone (BZ) sampling, we obtained zero-temperature energies converged to within 0.5 meV per formula unit. For the geometry relaxations, a force tolerance of  $0.005 \text{ eV} \cdot \text{\AA}^{-1}$  was imposed on all the atoms. The optoelectronic properties were estimated using hybrid functionals [29] (Supplementary Fig.3 and Supplementary Discussion) and considering spin-orbit coupling (SOC) effects, a computational approach named here as HSEsol+SOC. In this case, to make the calculations feasible, the energy cutoff and  $\mathbf{k}$ -point grid were slightly reduced to 550 eV and  $6 \times 6 \times 6$ , respectively. Quantum nuclear effects [56] were disregarded throughout this work.

All-electron DFT calculations were also performed with the WIEN2k package [58] using the local-density approximation (LDA) [59] to the exchange correlation energy along with the linearized augmented plane wave method (FP-LAPW) [60, 61]. The technical parameters for these calculations were a  $10 \times 10 \times 10$   $\mathbf{k}$ -point grid and a muffin-tin radius equal to  $R_{\text{MT}} = 7.0/K_{\text{max}}$ , where  $K_{\text{max}}$  represents the plane-wave cutoff. Localized energy-resolved Wannier states [62] were then obtained for the tight-binding calculations [63–65] considering the relevant Hilbert space in the interval  $-10 \leq E \leq 20 \text{ eV}$  around the Fermi energy.

**Finite-temperature first-principles simulations.** *Ab initio* molecular dynamics (AIMD) simulations were performed in the canonical  $(N, V, T)$  ensemble, neglecting thermal expansion effects and employing a large simulation cell containing 320 atoms with periodic boundary conditions applied along the three Cartesian directions. The temperature in the AIMD simulations

was kept fluctuating around a set-point value by using Nose-Hoover thermostats. Newton’s equations of motion were integrated using the standard Verlet’s algorithm with a time step of  $1.5 \cdot 10^{-3}$  ps.  $\Gamma$ -point sampling for reciprocal-space integration was employed in the AIMD simulations, which spanned approximately 100 ps. These calculations were performed with the semilocal PBEsol exchange-correlation functional [57].

**Harmonic phonon calculations.** The second-order interatomic force constant matrix of all CAP and resulting harmonic phonon spectrum were calculated with the finite-differences method as is implemented in the PhonoPy software [66]. Large supercells (i.e.,  $4 \times 4 \times 4$  for the cubic  $Pm\bar{3}m$  supercell containing 320 atoms) and a dense  $\mathbf{k}$ -point grid of  $3 \times 3 \times 3$  for BZ sampling were employed for the phonon calculations of targeted structures. Several numerical tests were conducted that demonstrated the adequacy of the selected  $\mathbf{k}$ -point grid. These calculations were performed with the semilocal PBEsol exchange-correlation functional [57].

**Anharmonic phonon calculations.** The DynaPhoPy code [67] was used to calculate the anharmonic lattice dynamics (i.e.,  $T$ -renormalized phonons) of CAP in the cubic  $Pm\bar{3}m$  phase from *ab initio* molecular dynamics (AIMD) simulations. A reduced  $2 \times 2 \times 2$  supercell and  $4 \times 4 \times 4$   $\mathbf{k}$ -point grid for BZ sampling were employed in the AIMD simulations to maintain high numerical accuracy (Supplementary Discussion and work [17]).

A normal-mode-decomposition technique was employed in which the atomic velocities  $\mathbf{v}_{jl}(t)$  ( $j$  and  $l$  represent particle and Cartesian direction indexes) generated during fixed-temperature AIMD simulation runs were expressed like:

$$\mathbf{v}_{jl}(t) = \frac{1}{\sqrt{Nm_j}} \sum_{\mathbf{q}s} \mathbf{e}_j(\mathbf{q}, s) e^{i\mathbf{q}\mathbf{R}_{jl}^0} v_{\mathbf{q}s}(t), \quad (7)$$

where  $N$  is the number of particles,  $m_j$  the mass of particle  $j$ ,  $\mathbf{e}_j(\mathbf{q}, s)$  a phonon mode eigenvector ( $\mathbf{q}$  and  $s$  stand for the wave vector and phonon branch),  $\mathbf{R}_{jl}^0$  the equilibrium position of particle  $j$ , and  $v_{\mathbf{q}s}$  the velocity of the corresponding phonon quasiparticle.

The Fourier transform of the autocorrelation function of  $v_{\mathbf{q}s}$  was then calculated, yielding the power spectrum:

$$G_{\mathbf{q}s}(\omega) = 2 \int_{-\infty}^{\infty} \langle v_{\mathbf{q}s}^*(0) v_{\mathbf{q}s}(t) \rangle e^{i\omega t} dt. \quad (8)$$

Finally, this power spectrum was approximated by a Lorentzian function of the form:

$$G_{\mathbf{q}s}(\omega) \approx \frac{\langle |v_{\mathbf{q}s}|^2 \rangle}{\frac{1}{2} \gamma_{\mathbf{q}s} \pi \left[ 1 + \left( \frac{\omega - \omega_{\mathbf{q}s}}{\frac{1}{2} \gamma_{\mathbf{q}s}} \right)^2 \right]}, \quad (9)$$

from which a  $T$ -renormalized quasiparticle phonon frequency,  $\omega_{\mathbf{q}s}(T)$ , was determined as the peak position,

and the corresponding phonon linewidth,  $\gamma_{\mathbf{qs}}(T)$ , as the full width at half maximum. These calculations were performed with the semilocal PBEsol exchange-correlation functional [57].

**Short-wavelength phonon band-gap correction.** The electron-phonon correction to the band gap due to the short-range phonon modes was computed as the difference between the band gap at zero temperature for the static structure and the average band gap obtained from AIMD simulations performed with a supercell, namely:

$$\Delta E_g^S(T) = \lim_{t_0 \rightarrow \infty} \frac{1}{t_0} \int_0^{t_0} E_g^{\mathbf{R}(t)} dt - E_g(0), \quad (10)$$

where  $\mathbf{R}$  represents the positions of the atoms in the supercell at a given time  $t$  of the AIMD simulation. This expression can be numerically approximated as shown in Eq. (3), where the band gap is averaged over a finite number,  $N$ , of configurations. Similarly, thermal effects on the dielectric tensor were computed.

These calculations were performed with the hybrid HSEsol exchange-correlation functional [29] and considering spin-orbit coupling effects (HSEsol+SOC). Due to involved high computational expense, the AIMD calculations were performed with a supercell containing 40 atoms and a  $\mathbf{k}$ -point mesh of a single point. The total number of configurations used for the average was  $N = 10$  for each material and temperature. These values were found to be appropriate for obtaining band-gap results accurate to within 0.1 eV (Supplementary Discussion).

**Long-wavelength phonon band-gap correction.** The electron-phonon correction to the band gap due to long-range phonon modes was computed using the Fröhlich equation for a three-dimensional polar material [33–36]. This correction was determined as the difference in the shifts of the conduction and valence bands, as given in Eq. (4), where the shift of each band was computed using the expression in Eq. (5). The physical quantities entering this latter expression were determined with DFT methods; the electron and hole effective masses were computed using the parabolic approximation at the maximum of the valence band and the minimum of the conduction band, respectively. For the LO phonon frequency, we used an effective value computed as the average of the three corresponding modes, as done in work [37]. Temperature-induced anharmonic effects were fully

taken into account for the calculation of these LO phonon frequencies.

The high-frequency and static dielectric constants, whose values were unusually large in static calculations, were recomputed as functions of temperature (using the same approach as we applied to the band gap and dielectric tensor) to capture thermal effects. We also considered the anisotropy of the dielectric tensor using the formula:

$$\frac{1}{\varepsilon_i} = \text{Tr}(\varepsilon_i^{-1})/3, \quad (11)$$

where  $\varepsilon$  represents the dielectric constant associated with the dielectric tensor  $\varepsilon$ .

## ACKNOWLEDGEMENTS

We acknowledge financial support by the Spanish Ministry of Science under the Grants No. TED2021-130265B-C22, TED2021-130265B-C21, No. PID2020-112975 GB-I00, No. RYC2018-024947-I and by the Generalitat de Catalunya under the Grants No. 2021SGR-00343 and No. 2021SGR-01519. Computational support was provided by the Red Española de Supercomputación under the Grants No. FI-2023-2-0004, FI-2023-3-0043, FI-2024-1-0005 and FI-2024-2-0003. This work is part of the Maria de Maeztu Units of Excellence Programme CEX2023-001300-M funded by MCIN/AEI (10.13039/501100011033). P.B. acknowledges support from the predoctoral program AGAUR-FI ajuts (2024 FI-1 00070) Joan Oró, which is backed by the Secretariat of Universities and Research of the Department of Research and Universities of the Generalitat of Catalonia, as well as the European Social Plus Fund. C.L. acknowledges support from the Spanish Ministry of Science, Innovation and Universities under an FPU grant. E.S. is grateful to the ICREA Academia program. Work at LIST was supported by the Luxembourg National Research Fund through grant C21/MS/15799044/FERRODYNAMICS. This project received funding from the European Union’s H2020 European Research Council under the grant agreement number 866018 (SENSATE). S.C. and B.M. are supported by a EPSRC grant [EP/V062654/1] and R.J. and B.M. are supported by a UKRI Future Leaders Fellowship [MR/V023926/1]. B.M. also acknowledges support from the Gianna Angelopoulos Programme for Science, Technology, and Innovation, and from the Winton Programme for the Physics of Sustainability.

[1] Giustino, F. Electron-phonon interactions from first principles. *Rev. Mod. Phys.* **89**, 015003 (2017).

[2] Lin, Z., Zhigilei, L.V. and Celli, V. Electron-phonon coupling and electron heat capacity of metals under conditions of strong electron-phonon nonequilibrium. *Phys.*

- Rev. B* **77**, 075133 (2008).
- [3] Bohnen, K.-P., Heid, R. and Renker, B. Phonon dispersion and electron-phonon coupling in MgB<sub>2</sub> and AlB<sub>2</sub>. *Phys. Rev. Lett.* **86**, 5771 (2001).
- [4] Monserrat, B., Park, J.-S. and Walsh, A. Role of electron-phonon coupling and thermal expansion on band gaps, carrier mobility, and interfacial offsets in kesterite thin-film solar cells. *Appl. Phys. Lett.* **112**, 193903 (2018).
- [5] Monserrat, B. and Vanderbilt, D. Temperature dependence of the bulk Rashba splitting in the bismuth tellurohalides. *Phys. Rev. Mater.* **1**, 054201 (2017).
- [6] Varshni, Y. P. Temperature dependence of the energy gap in semiconductors. *Physica* **34**, 149 (1967).
- [7] O'Donnell, K. P. and Chen, X. Temperature dependence of semiconductor band gaps. *Appl. Phys. Lett.* **58**, 2924 (1991).
- [8] Poncé, S., Gillet, Y., Janssen, J.L., Marini, A., Verstraete, M. and Gonze, X. Temperature dependence of the electronic structure of semiconductors and insulators. *J. Chem. Phys.* **143**, 102813 (2015).
- [9] Park, J., Saidi, W.A., Chorpening, B. and Duan, Y. Applicability of Allen-Heine-Cardona theory on MO<sub>x</sub> metal oxides and ABO<sub>3</sub> perovskites: Toward high-temperature optoelectronic applications. *Chem. Mater.* **34**, 6108 (2022).
- [10] Giustino, F., Louie, S.G. and Cohen, M. L. Electron-phonon renormalization of the direct band gap of diamond. *Phys. Rev. Lett.* **105**, 265501 (2010).
- [11] Monserrat, B., Drummond, N.D. and Needs, R.J. Anharmonic vibrational properties in periodic systems: energy, electron-phonon coupling, and stress. *Phys. Rev. B* **87**, 144302 (2013).
- [12] Liu, Y., Monserrat, B. and Wiktor, J. Strong electron-phonon coupling and bipolarons in Sb<sub>2</sub>S<sub>3</sub>. *Phys. Rev. Mater.* **7**, 085401 (2023).
- [13] Monserrat, B., Engel, E.A. and Needs, R.J. Giant electron-phonon interactions in molecular crystals and the importance of nonquadratic coupling. *Phys. Rev. B* **92**, 140302 (2015).
- [14] Villegas, C.E.P., Rocha, A.R. and Marini, A. Anomalous temperature dependence of the band gap in black phosphorus. *Nano Lett.* **16**, 5095 (2016).
- [15] Saidi, W.A., Poncé, S. and Monserrat, B. Temperature dependence of the energy levels of methylammonium lead iodide perovskite from first-principles. *J. Phys. Chem. Lett.* **7**, 5247 (2016).
- [16] Artus, L. and Bertrand, Y. Anomalous temperature dependence of fundamental gap of AgGaS<sub>2</sub> and AgGaSe<sub>2</sub> chalcopyrite compounds. *Sol. Stat. Commun.* **61**, 733 (1987).
- [17] Benítez, P., López, C., Liu, C., Caño, I., Tamarit, J.-Ll., Saucedo, E. and Cazorla, C. Crystal structure prediction and phase stability in highly anharmonic silver-based chalcogenide anti-perovskites. arXiv:2406.04966 (2024).
- [18] Takahashi, T. and Yamamoto, O. The Ag/Ag<sub>3</sub>SI/I<sub>2</sub> solid-electrolyte cell. *Electrochim. Acta* **11**, 779 (1966).
- [19] Hull, S. Superionics: crystal structures and conduction processes. *Rep. Prog. Phys.* **67**, 1233 (2004).
- [20] Wakamura, K., Miura, F., Kojima, A. and Kanashiro, T. Observation of anomalously increasing phonon damping constant in the  $\beta$  phase of the fast-ionic conductor Ag<sub>3</sub>SI. *Phys. Rev. B* **41**, 2758 (1990).
- [21] Sakuma, T. Treatment of anharmonic thermal vibration by using transformation of scattering vector. *J. Phys. Soc. Jpn.* **54**, 4188 (1985).
- [22] Kawamura, J., Shimoji, M. and Hoshino, H. The ionic conductivity and thermoelectric power of the superionic conductor Ag<sub>3</sub>SBr. *J. Phys. Soc. Jpn.* **50**, 194 (1981).
- [23] Magistris, A., Pezzati, E. and Sinistri, C. Thermoelectric properties of high-conductivity solid electrolytes. *Z. Naturforsch.* **27a**, 1379 (1972).
- [24] Palazon, F. Metal chalcogenides: Next generation photovoltaic materials? *Sol. RRL* **6**, 2100829 (2022).
- [25] Ghorpade, U.V., Suryawanshi, M. P., Green, M. A., Wu, T., Hao, X. and Ryan, K. M. Emerging chalcogenide materials for energy applications. *Chem. Rev.* **123**, 327 (2023).
- [26] Sebastiá-Luna, L., Rodkey, N., Mirza, A. S., Mertens, S., Lal, Melchor, A., Carranza, G., Calbo, J., Righetto, M., Sessolo, M., Herz, L. M., Vandewal, K., Ortí, E., Morales-Masis, M., Bolink, H. J. and Palazon, F. Chalcogenide antiperovskite thin films with visible light absorption and high charge-carrier mobility processed by solvent-free and low-temperature methods. *Chem. Mater.* **35**, 6482 (2023).
- [27] Caño, I., Turnley, J. W., Benítez, P., López-Álvarez, C., Asensi, J.-M., Payno, D., Puigdollers, J., Placidi, M., Cazorla, C., Agrawal, R. and Saucedo, E. Novel synthesis of semiconductor chalcogenide anti-perovskites by low-temperature molecular precursor ink deposition methodologies. *J. Mater. Chem. C* **12**, 3154 (2024).
- [28] Liu, Z., Mi, R., Ji, G., Liu, Y., Fu, P., Hu, S., Xia, B. and Xiao, Z. Bandgap engineering and thermodynamic stability of oxyhalide and chalcogenide antiperovskites. *Ceram. Int.* **47**, 32634 (2021).
- [29] Krukau, A. V., Vydrov, O. A., Izmaylov, A. F., Scuseria, G. E. Influence of the exchange screening parameter on the performance of screened hybrid functionals. *J. Chem. Phys.* **125**, 224106 (2006).
- [30] Sakuma, T. and Hoshino, S. The phase transition and the structures of superionic conductor Ag<sub>3</sub>SBr. *J. Phys. Soc. Jpn.* **49**, 678 (1980).
- [31] Hoshino, S., Fujishita, H., Takashige, M. and Sakuma, T. Phase transition of Ag<sub>3</sub>SX (X= I, Br). *Solid State Ion.* **3**, 35 (1981).
- [32] Cho, N., Kikkawa, S., Kanamaru, F. and Yoshiasa, A. Structural refinement of Ag<sub>3</sub>SI by single crystal X-ray diffraction method. *Solid State Ion.* **68**, 57 (1994).
- [33] Zacharias, M., Scheffler, M. and Carbogno, C.. Fully anharmonic nonperturbative theory of vibronically renormalized electronic band structures. *Phys. Rev. B* **102**, 045126 (2020).
- [34] Chen, S., Parker, I. J. and Monserrat, B. Temperature effects in topological insulators of transition metal dichalcogenide monolayers. *Phys. Rev. B* **109**, 155125 (2024).
- [35] Poncé, S., Gillet, Y., Janssen, J. L., Marini, A., Verstraete, M. and Gonze, X. Temperature dependence of the electronic structure of semiconductors and insulators. *J. Chem. Phys.* **143**, 102813 (2015).
- [36] Zacharias, M. and Giustino, F. Theory of the special displacement method for electronic structure calculations at finite temperature. *Phys. Rev. Res.* **2**, 013357 (2020).
- [37] Melo, P. M., Abreu, J. C., Guster, B., Giantomassi, M., Zanoli, Z., Gonze, X. and Verstraete, M. J. High-throughput analysis of Fröhlich-type polaron models. *npj Comput. Mater.* **9**, 147 (2023).

- [38] Wang, V., Xu, N., Liu, J. C., Tang, G., Geng, W. T. VASPKIT: A user-friendly interface facilitating high-throughput computing and analysis using VASP code. *Comput. Phys. Commun.* **267**, 108033 (2021).
- [39] Cohen, R. E. Origin of ferroelectricity in perovskite oxides. *Nature* **358**, 136 (1992).
- [40] Zhong, W., Vanderbilt, D. and Rabe, K. M. Phase transitions in BaTiO<sub>3</sub> from first principles. *Phys. Rev. B* **73**, 1861 (1994).
- [41] Jain, A., Ong, S. P., Hautier, G. *et al.* The Materials Project: A materials genome approach to accelerating materials innovation. *APL Mater.* **1**, 011002 (2013).
- [42] <https://github.com/atztogo/phonondb>
- [43] Berger, R. F., Fennier, C. J. and Neaton, J. B. Band gap and edge engineering via ferroic distortion and anisotropic strain: The case of SrTiO<sub>3</sub>. *Phys. Rev. Lett.* **107**, 146804 (2011).
- [44] S.H. Wemple. Polarization fluctuations and the optical-absorption edge in BaTiO<sub>3</sub>. *Phys. Rev. B* **2**, 2679 (1970).
- [45] Evarestov, R. A. and Bandura, A. V. First-principles calculations on the four phases of BaTiO<sub>3</sub>. *J. Comput. Chem.* **33**, 1123 (2012).
- [46] Weber, M. C., Guennou, M., Toulouse, C., Cazayous, M., Gillet, Y., Gonze, X. Kreisel, J. Temperature evolution of the band gap in BiFeO<sub>3</sub> traced by resonant Raman scattering. *Phys. Rev. B* **93**, 125204 (2016).
- [47] Cazorla, C. and Íñiguez-González, J. Insights into the phase diagram of bismuth ferrite from quasiharmonic free-energy calculations. *Phys. Rev. B* **88**, 214430 (2013).
- [48] Kennes, D., Wilner, E., Reichman, D. *et al.* Transient superconductivity from electronic squeezing of optically pumped phonons. *Nat. Phys.* **13**, 479 (2017).
- [49] Dekorsky, T., Kütt, W., Pfeifer, T. and Kurz, H. Coherent control of LO-phonon dynamics in opaque semiconductors by femtosecond laser pulses. *Europhys. Lett.* **23**, 223 (1993).
- [50] Pomarico, E., Mitrano, M., Bromberger, H. *et al.* Enhanced electron-phonon coupling in graphene with periodically distorted lattice. *Phys. Rev. B* **95**, 024304 (2017).
- [51] Qi, Y., Liu, S., Lindenberg, A. M. and Rappe, A. M. Ultrafast electric field pulse control of giant temperature change in ferroelectrics. *Phys. Rev. Lett.* **120**, 055901 (2018).
- [52] Peng, B., Hu, Y., Murakami, S., Zhang, T. and Monserrat, B. Topological phonons in oxide perovskites controlled by light. *Sci. Adv.* **6**, eabd1618 (2020).
- [53] Rurali, R., Escorihuela-Sayalero, C., Tamari, J.-Ll., Íñiguez-González, J. and Cazorla, C. Giant photocaloric effects across a vast temperature range in ferroelectric perovskites. *Phys. Rev. Lett.* **133**, 116401 (2024).
- [54] Kresse, G. and Furthmüller, J. Efficient iterative schemes for ab initio total-energy calculations using a plane-wave basis set. *Phys. Rev. B* **54**, 11169 (1996).
- [55] Blöchl, P. E. Projector augmented-wave method. *Phys. Rev. B* **50**, 17953 (1994).
- [56] Cazorla, C. and Boronat, J. Simulation and understanding of atomic and molecular quantum crystals. *Rev. Mod. Phys.* **89**, 035003 (2017).
- [57] Perdew, J. P., Ruzsinszky, A., Csonka, G. I. *et al.* Restoring the density-gradient expansion for exchange in solids and surfaces. *Phys. Rev. Lett.* **100**, 136406 (2008).
- [58] Blaha, P., Karlheinz, S., Fabien, T., Laskowski, R., Georg, M. and Laurence, D. M. WIEN2k: An APW+lo program for calculating the properties of solids. *The Journal of Chemical Physics* **152**, 074101 (2020).
- [59] Perdew, J. P. and Wang, Y. Accurate and simple analytic representation of the electron-gas correlation energy. *Phys. Rev. B* **45**, 13244 (1992).
- [60] David, J. S. Planewaves, pseudopotentials and the LAPW method. *Springer New York, NY* (2006).
- [61] Blaha, P., Schwarz, K., Sorantin, P. and Trickey, S. B. Full-potential, linearized augmented plane wave programs for crystalline systems. *Comput. Phys. Commun.* **59**, 399 (1990).
- [62] Marzari, N. and Vanderbilt, D. Maximally localized generalized Wannier functions for composite energy bands. *Phys. Rev. B* **56**, 12847 (1997).
- [63] Wei, K., Rosner, H., Pickett, W. E. and Scalettar, R. T. Insulating ferromagnetism in La<sub>4</sub>Ba<sub>2</sub>Cu<sub>2</sub>O<sub>10</sub>: An ab initio Wannier function analysis. *Phys. Rev. Lett.* **89**, 167204 (2002).
- [64] Wei-Guo, Y., Volja, D. and Wei, K. . Orbital ordering in LaMnO<sub>3</sub>: Electron-electron versus electron-lattice interactions. *Phys. Rev. Lett.* **96**, 116405 (2006).
- [65] Ruoshi, J., Lang, Z.-J., Berlijn, T. and Ku, W. Variation of carrier density in semimetals via short-range correlation: A case study with nickelate NdNiO<sub>2</sub>. *Phys. Rev. B* **108**, 155126 (2023).
- [66] Togo, A. and Tanaka, I. First principles phonon calculations in materials science. *Scr. Mater* **108**, 1 (2015).
- [67] Carreras, A., Togo, A. and Tanaka, I. DynaPhoPy: A code for extracting phonon quasiparticles from molecular dynamics simulations. *Comput. Phys. Commun.* **221**, 221 (2017).